Exploring Complex Neuronal Dynamics Using Atangana–Baleanu Fractal-Fractional Order Morris–Lecar Model

M. J. Abedin[1*], M. J. Islam[2], M. G. Hafez[2*] and Yu-Ming Chu[3,4*]

[1]Department of Biomedical Engineering, Chittagong University of Engineering and Technology, Chattogram - 4349, Bangladesh.

[2]Department of Mathematics, Chittagong University of Engineering and Technology, Chattogram - 4349, Bangladesh.

[3]Department of Mathematics, Huzhou University, Huzhou, 313000 China.

[4]Institute for Advanced Study Honoring Chen Jian Gong, Hangzhou Normal University, Hangzhou 311121 China.

*Corresponding Email: joynulabedin@cuet.ac.bd (M. J. A.); hafez@cuet.ac.bd (M. G. H.); chuyuming@zjhu.edu.cn (Y-M. C.)

Abstract

Fractal-fractional calculus offers a powerful framework for modeling physical and biological systems that exhibit memory-dependent behavior. Unlike traditional calculus, it employs differential and integral operators of non-integer order, allowing it to capture dynamics associated with systems possessing fractional or fractal properties. Given the capacity of fractal-fractional derivatives to effectively represent long-term memory effects in neural responses, we extend the classical Morris–Lecar model into the fractal-fractional order domain to better describe the dynamics of neuronal activity. This generalized Atangana–Baleanu fractal-fractional order Morris–Lecar (FFML) model is constructed to explore the complex spiking behavior inherent to neuron systems, and its performance is compared with that of the original integer-order model. Since exact analytical solutions of the FFML model are generally not obtainable, we rely on numerical approximation techniques to study its behavior. Our simulations reveal that, depending on the fractional derivative order $\alpha \in (0,1)$ with fractal time dimension $\tau \in (0,1)$ and input current levels, the model is capable of exhibiting a wide range of dynamics, including quiescent states, regular spiking, and bursting patterns—similar to the classical model but under different parameter regimes. Furthermore, we identify several bifurcation phenomena in the fractional-order, fractal-dimensional, or both fractal- fractional system by varying the input current and the order of the derivative and time dimension. By tuning the fractional order and fractal-dimension, we are able to classify different dynamical regimes of the model. This enhanced flexibility provides a richer understanding of the complex behaviors exhibited by single neuron systems, making the fractal-fractional approach a valuable tool in computational neuroscience.

Keywords: Atangana–Baleanu Fractal-fractional operator; Morris–Lecar Model; Numerical approximation; Neuronal Dynamics.

1. INTRODUCTION

Nonlinear dynamical systems play a crucial role in the study of computational neuroscience [1-10]. A landmark observation was made by Hodgkin in 1948, who found that neurons could respond to a direct current (DC) stimulus in different ways [1,5-7]. Specifically, some neurons fired repetitively even with very small currents, while others only spiked within a narrow range of current values. This phenomenon sparked further research by Rinzel and Ermentrout, who demonstrated that such variations in neuronal responses could be explained by different bifurcation mechanisms underlying excitability [8, 9]. When considering the externally applied current, denoted as I_{app}, as a control parameter, it becomes evident that neuron dynamics can shift significantly. At low values of I_{app}, the neuron typically stays at rest.

However, as I_{app} increases, a critical point is reached where the system undergoes a bifurcation—transitioning from a stable equilibrium state to a periodic limit cycle. This transition marks the onset of repetitive firing or spiking activity [8-10].

However, fractional calculus has gained significant attention across multiple scientific fields, including biology, physics, chemistry, hydrology, medicine, and finance [1-6]. Its growing use in modeling complex systems has led to a surge in related research publications. One of the key features of fractional-order derivatives is their ability to account for the "memory effect," a property where the current state of a system depends not only on its present conditions but also on its past states [2, 6]. Experimental studies have shown that fractional differential and integral equations offer a more accurate representation of the behavior of certain biological and physical systems than traditional integer-order models. These systems often display characteristics such as fractality and long-term memory, which are naturally captured by fractional-order approaches. Additional, fractal calculus is relatively new, it can effectively deal with kinetics, which is always called as the fractal kinetics [11, 12], where the fractal time replaces the continuous time. Notably revealed that time does be discontinuous in microphysics [13], that means that fractal kinetics takes place on very small time scale. To better understand the concept, Figures 1 and 2 illustrate the differences between classical gradients and newer approaches such as fractal and fractional gradients. Figure 1 shows a classical linear gradient between points A and B. However, it also highlights how this approach fails when applied to rough or jagged paths, like those seen in fractal geometries. This visual clearly demonstrates why a new concept—the fractal gradient—is necessary when dealing with irregular or discontinuous shapes, where classical methods break down. Figure 2 compares different types of system responses. The blue line represents a simple, memoryless system that responds instantly to changes in input, without being influenced by its past. In contrast, the red line shows a system governed by fractional calculus, where past states influence current behavior. This results in a more irregular and noisy output, similar to what is observed in many real-world processes, such as biological systems. The green line represents a smoothed version of the fractional response, created by applying a low-pass filter (like a moving average). This simulates how systems with memory do not react instantly but are instead influenced by a history of past inputs. These observations suggest that to accurately model and analyze complex physical systems, it is essential to go beyond classical methods and incorporate fractal, fractional, and even fractal-fractional calculus.

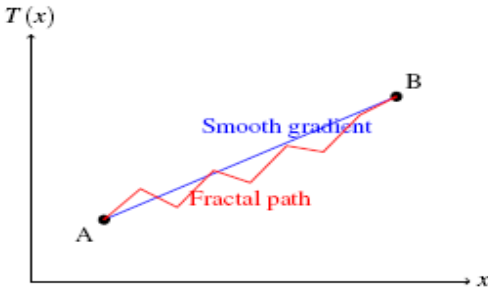

Fig. 1 Fractal gradient. In smooth space (blue), the gradient between A and B is defined by a straight slope. In fractal space (red), the irregular path requires a new definition of gradient.

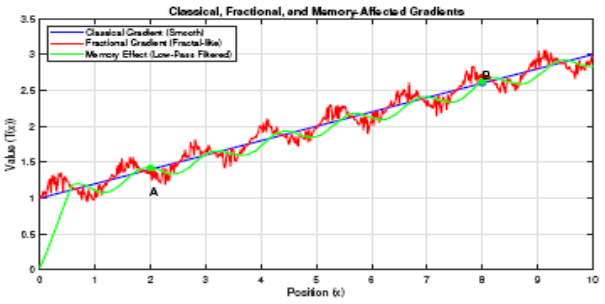

Fig. 2 Fractional gradient versus classical gradient. The smooth line (blue) illustrates the classical gradient defined over continuous space, while the jagged red line represents a fractional (fractal-like) gradient, emphasizing the need for a generalized gradient concept in discontinuous or complex media.

In the context of neuroscience, this complexity-driven perspective has led to the integration of ideas

from fractal geometry and nonlinear dynamics. This interdisciplinary approach is proving valuable for understanding and regulating the behavior of complex neuronal processes [7, 8]. As discussed by Moaddy et al [14], fractional-order models offer a better explanation of the long-term memory effects observed in neuronal responses. A notable feature of neural systems is their ability to adapt to changes in external stimuli. While traditional models suggest that a single neuron adapts over a single time scale, research has identified neurons that exhibit adaptation over multiple time scales [15]. This behavior aligns well with fractional-order dynamics, where the firing rate of a neuron can be modeled as a fractional derivative of slowly varying input parameters. One of the key advantages of using fractional derivatives in neuronal modeling is their ability to naturally incorporate adaptation over multiple temporal scales. Additionally, Shi et al. [16] demonstrated that fractional derivatives can accurately represent dielectric properties and memory effects in biological structures such as membranes and cells. Their findings suggest that non-integer derivatives can facilitate faster activation of slow ion channels and promote rapid spiking activity, which contributes to the emergence of diverse bursting patterns. Another important property of fractional-order models is their capacity to exhibit both chaotic and periodic firing behaviors under the same parameter settings, solely by altering the order of the derivative [17]. This introduces a new degree of freedom in controlling neuronal activity. By treating the fractional order, itself as a tunable parameter, researchers have found enhanced flexibility in regulating the behavior of neural systems [18]. Due to these features—such as memory representation, multi-scale adaptation, and dynamic flexibility—fractional-order models have become a powerful tool in computational neuroscience. They have been successfully applied in several neuron models, including the fractional cable model, the Izhikevich neuron model, and the FitzHugh-Rinzel bursting model [19, 20]. Although Azizi [21] utilized the Grünwald-Letnikov (GL) fractional derivative to generalize the Morris-Lecar model, the GL approach is often criticized for its limited numerical stability and high computational cost in long-time simulations. These drawbacks can obscure fine-scale neuronal dynamics, especially when modeling long-term memory effects inherent in biological systems.

Given the inherent complexity of the nervous system, traditional integer-order models often fall short in capturing the full range of neuronal behaviors and properties. Additionally, models incorporating [21], Riemann–Liouville [22] and Caputo [23], or conformable [24, 25] fractional derivatives often also fall short in capturing the full range of neuronal behaviors due to some limitation of these derivatives. To overcome these limitations, this study employs fractal-fractional calculus [26-30] as a mathematical framework to analyze the fractal-like dynamics of neuronal processes. Specifically, we apply this approach to the Morris–Lecar model [21, 31], a simplified version of the Hodgkin–Huxley model that retains essential features of neuronal excitability. While many researchers have incorporated fractional derivatives—such as Grunwald–Letnikov, Riemann–Liouville (RL), Caputo, or conformable derivatives—into neuron models to study their dynamic behavior. To the best of our knowledge, no previous work has generalized the integer-order Morris–Lecar model into the fractal-fractional domain for a more accurate representation of neuronal dynamics. The Morris–Lecar model is well known for reproducing key phenomena such as action potential generation, threshold dynamics, and sustained oscillations in response to external stimuli. Its reduced complexity makes it a suitable candidate for exploring the benefits of fractal-fractional order modeling. In this study, we proposed a fractal-fractional-order Morris–Lecar model (FFMLM) to more accurately simulate the spiking behavior and physiological characteristics of a single neuron. Since analytical solutions to the FFMLM are generally unavailable, we employ numerical methods to approximate its behavior. The dynamics of the fractional model are then compared with those of the classical integer-order version using phase portrait analysis.

2. BACKGROUND OF ATANGANA–BALEANU FRACTAL-FRACTIONAL CALCULUS

To aid in understanding, this section briefly introduces several important concepts from AB fractal–fractional calculus, based on references [26-30].

Definition 1. Suppose $\mathcal{Y}(t)$ is continuous and fractally differentiable on the interval (a, b) with order τ. The fractal–fractional derivative of $\mathcal{Y}(t)$ of order α in the Riemann–Liouville sense, involving a generalized Mittag-Leffler kernel, is defined as:

$$^{\mathcal{FFM}}\mathcal{D}_{0,t}^{\alpha,\tau}\mathcal{Y}(t) = \frac{\mathcal{AB}(\alpha)}{1-\alpha}\frac{d}{dt^{\tau}}\int_0^t \mathcal{E}_{\alpha}\Big(-\frac{\alpha}{1-\alpha}(t-\mathcal{S})^{\alpha}\Big)\mathcal{Y}(\mathcal{S})d\mathcal{S}. \tag{1}$$

where $0 < \alpha, \tau \leq 1$, $\mathcal{AB}(\alpha)$ is defined as $\mathcal{AB}(\alpha) = (1-\alpha) + \alpha/\Gamma(\alpha)$ and $\mathcal{E}_{\alpha}(.)$ denotes the generalized Mittag-Leffler function, defined by $\mathcal{E}_{\alpha}(z) = \sum_{k=0}^{\infty} z^k/\Gamma(\alpha k + 1)$, $\alpha > 0$, $z \in \mathbb{C}$.This function generalizes the exponential function and frequently appears in solutions of fractional differential equations.

Definition 2. Suppose that $\mathcal{Y}(t)$ is continuous on an open interval (a, b). Then, the fractal--fractional integral of order α, with a generalized Mittag-Leffler type kernel, is defined as:

$$^{\mathcal{FFM}}\mathcal{D}_{0,t}^{\alpha,\tau}\mathcal{Y}(t) = \frac{\alpha\tau}{\mathcal{AB}(\alpha)}\int_0^t \mathcal{S}^{\tau-1}\mathcal{Y}(\mathcal{S})(t-\mathcal{S})^{\alpha-1}\,d\mathcal{S} + \frac{\tau(1-\alpha)t^{\tau-1}\mathcal{Y}(t)}{\mathcal{AB}(\alpha)}. \tag{2}$$

This definition incorporates a memory effect through the convolution-type integral and a fractal scaling via the parameters α and τ.

Definition 3. The fractal derivative of $\mathcal{Y}(t)$ with order τ is

$$\frac{d\mathcal{Y}(\mathcal{S})}{d\mathcal{S}^{\tau}} = \lim_{t\to\mathcal{S}}\frac{\mathcal{Y}(t)-\mathcal{Y}(\mathcal{S})}{t^{\tau}-\mathcal{S}^{\tau}}. \tag{3}$$

For implementation, an ordinary differential equation involving a fractal--fractional derivative in the Atangana--Baleanu sense is considered as

$$^{\mathcal{FFM}}\mathcal{D}_{0,t}^{\alpha,\tau}\mathcal{F}(t) = \mathfrak{X}\big(t, \mathcal{F}(t)\big). \tag{4}$$

According to the definition of the AB fractal-fractional derivative, the above equation can be simplified as

$$\frac{\mathcal{AB}(\alpha)}{1-\alpha}\frac{d}{dt^{\tau}}\int_0^t \mathcal{E}_{\alpha}\Big(-\frac{\alpha}{1-\alpha}(t-\mathcal{S})^{\alpha}\Big)\mathfrak{X}\big(\mathcal{S}, \mathcal{F}(\mathcal{S})\big)d\mathcal{S} = \psi(\mathrm{t})\mathfrak{X}\big(t, \mathcal{F}(t)\big). \tag{5}$$

where $\psi(\mathrm{t}) = \tau\, \mathrm{t}^{\,\tau-1}$ is a time-scaling term related to the fractal structure (interpretation may depend on the context).

3. FRACTAL-FRACTIONAL MODELING FOR NEURONAL DYNAMICS

In 1981, Kathleen Morris and Harold Lecar [31] proposed the Morris–Lecar model, a simplified mathematical representation aimed at capturing the fundamental mechanisms underlying action potential generation in neurons. This model is a reduced form of the more complex four-dimensional Hodgkin–Huxley model, retaining its essential physiological features while offering a more tractable framework for mathematical analysis and numerical simulation [31-33]. The Morris–Lecar model describes neuronal dynamics through a system of two coupled nonlinear ordinary differential equations and incorporates three key ion channels: a calcium channel, which contributes to membrane depolarization; a potassium channel, responsible for repolarization; and a leak channel, which maintains resting membrane potential. Due to its balance between biological realism and computational simplicity, the Morris–Lecar model has become a widely used tool in theoretical neuroscience for studying neuronal excitability, bifurcation behavior, and pattern formation. To extend the classical Morris--Lecar model into the framework of fractional calculus, we begin by considering the total membrane current as the sum of the ionic and capacitive currents. This relationship is defined as $I_{app} = I_{ion} + I_{CM}$ based on ref. [34] , where I_{app} is the externally applied current, I_{ion} denotes the sum of all ionic currents, and I_{CM} represents the capacitive current. In the fractal-fractional order version of the model, the capacitive current is redefined to incorporate memory effects and geometrical changes through a fractal-fractional derivative. Specifically, we express I_{CM} as $I_{CM} = C_M {}^{\mathcal{FFM}}\mathcal{D}_{0,t}^{\alpha,\tau} V(t)$, where C_M is the membrane capacitance, $V(t)$ is the membrane potential, and ${}^{\mathcal{FFM}}\mathcal{D}_{0,t}^{\alpha,\tau}$ denotes a AB fractal-fractional derivative of order α, with dimension τ. The choice of the ${}^{\mathcal{FFM}}\mathcal{D}_{0,t}^{\alpha,\tau}$ depends on the mathematical properties and physical interpretation desired in the modeling context. Thus, the AB FFMLM describes the dynamics of V and a recovery variable N is defined in the following forms:

$$\begin{aligned} C_M {}^{\mathcal{FFM}}\mathcal{D}_{0,t}^{\alpha,\tau} V(t) &= I_{app} - g_{ca}\mathcal{P}_\infty(V)(V - V_{ca}) - g_K N(V - V_K) - g_L(V - V_L), \\ {}^{\mathcal{FFM}}\mathcal{D}_{0,t}^{\alpha,\tau} N(t) &= \phi(\mathcal{L}_\infty(V) - N)/\mathcal{W}(V), \end{aligned} \tag{6}$$

where

$$\begin{aligned} \mathcal{P}_\infty(V) &= \frac{1}{2}\left(1 + \tanh\left(\frac{V - V_1}{V_2}\right)\right), \\ \mathcal{L}_\infty(V) &= \frac{1}{2}\left(1 + \tanh\left(\frac{V - V_3}{V_4}\right)\right), \\ \mathcal{W}(V) &= \frac{1}{\cosh\left(\frac{V - V_3}{2V_4}\right)}. \end{aligned} \tag{7}$$

Here, g_{ca}, g_K and g_L are the maximal conductances for calcium, potassium, and leak channels; V_{ca}, $V_K$and V_L are the reversal potentials for calcium, potassium, and leak channels; V_1, V_2, V_3 and V_4 are the parameters determining the shape of the activation/inactivation functions; and ϕ is the scaling factor for the recovery variable dynamics.

4. NUMERICAL SCHEME FOR THE ATANGANA--BALEANU FRACTAL--FRACTIONAL DERIVATIVE

In this section, we develop a numerical scheme for the proposed differential models that involve the Atangana--Baleanu fractal--fractional derivative based on the reference [26]. Specifically, we consider systems where the fractional operator is defined in the sense of Atangana and Baleanu, incorporating both nonlocal and nonsingular kernel effects along with fractal properties. To construct the numerical method, we begin with the considered model defined in Eq. (6), and rewrite the system in a form compatible with the Atangana--Baleanu fractal--fractional framework. This representation enables us to

apply appropriate discretization techniques tailored to the memory-preserving and nonlocal structure of the operator. The model equation can be reformulated using the Atangana--Baleanu fractal--fractional derivative as:

$$C_M{}^{\mathcal{FFM}}\mathcal{D}_{0,t}^{\alpha,\tau}V(t) = t^{\tau-1}\tau\mathcal{V}(V,N,t),$$
$$^{\mathcal{FFM}}\mathcal{D}_{0,t}^{\alpha,\tau}N(t) = t^{\tau-1}\tau\mathcal{N}(V,N,t), \quad (8)$$

By implementing AB FI on both sides, one obtains

$$\boldsymbol{V(t) = V(0) + \frac{\tau(1-\alpha)t^{\tau-1}}{\mathcal{AB}(\alpha)}\mathcal{V}(V,N,t) + \frac{\tau\alpha}{\mathcal{AB}(\Gamma(\alpha))}\int_0^t \mathcal{S}^{\tau-1}(t-\mathcal{S})^{\alpha-1}\mathcal{V}(V,N,\mathcal{S},t)d\mathcal{S}}, \quad (9)$$

$$\boldsymbol{N(t) = N(0) + \frac{\tau(1-\alpha)t^{\tau-1}}{\mathcal{AB}(\alpha)}\mathcal{N}(V,N,t) + \frac{\tau\alpha}{\mathcal{AB}(\Gamma(\alpha))}\int_0^t \mathcal{S}^{\tau-1}(t-\mathcal{S})^{\alpha-1}\mathcal{N}(V,N,\mathcal{S},t)d\mathcal{S}}, \quad (10)$$

For $\boldsymbol{t_{\mathcal{R}+1}}$, one obtains

$$\boldsymbol{V^{\mathcal{R}+1}(t) = V^0 + \frac{\tau(1-\alpha)t_{\mathcal{R}}{}^{\tau-1}}{\mathcal{AB}(\alpha)}\mathcal{V}(V^{\mathcal{R}},N^{\mathcal{R}},t_{\mathcal{R}}) + \frac{\tau\alpha}{\mathcal{AB}(\alpha)(\Gamma(\alpha))}\int_0^{t_{\mathcal{R}+1}} \mathcal{S}^{\tau-1}(t_{\mathcal{R}+1}-\mathcal{S})^{\alpha-1}\mathcal{V}(V,N,\mathcal{S},t)d\mathcal{S}}, \quad (11)$$

$$\boldsymbol{N^{\mathcal{R}+1}(t) = N^0 + \frac{\tau(1-\alpha)t_{\mathcal{R}}{}^{\tau-1}}{\mathcal{AB}(\alpha)}\mathcal{N}(V^{\mathcal{R}},N^{\mathcal{R}},t_{\mathcal{R}}) + \frac{\tau\alpha}{\mathcal{AB}(\alpha)(\Gamma(\alpha))}\int_0^{t_{\mathcal{R}+1}} \mathcal{S}^{\tau-1}(t_{\mathcal{R}+1}-\mathcal{S})^{\alpha-1}\mathcal{N}(V,N,\mathcal{S},t)d\mathcal{S}}, \quad (12)$$

The above system can be expressed as, using the approximation of the integrals,

$$\boldsymbol{V^{\mathcal{R}+1}(t) = V^0 + \frac{\tau(1-\alpha)t_{\mathcal{R}}{}^{\tau-1}}{\mathcal{AB}(\alpha)}\mathcal{V}(V^{\mathcal{R}},N^{\mathcal{R}},t_{\mathcal{R}}) + \frac{\tau\alpha}{\mathcal{AB}(\alpha)(\Gamma(\alpha))}\sum_{r=0}^{\mathcal{R}}\int_0^{t_{\mathcal{R}+1}} \mathcal{S}^{\tau-1}(t_{\mathcal{R}+1} - \mathcal{S})^{\alpha-1}\mathcal{V}(V,N,\mathcal{S},t)d\mathcal{S}}, \quad (13)$$

$$\boldsymbol{N^{\mathcal{R}+1}(t) = N^0 + \frac{\tau(1-\alpha)t_{\mathcal{R}}{}^{\tau-1}}{\mathcal{AB}(\alpha)}\mathcal{N}(V^{\mathcal{R}},N^{\mathcal{R}},t_{\mathcal{R}}) + \frac{\tau\alpha}{\mathcal{AB}(\alpha)(\Gamma(\alpha))}\sum_{r=0}^{\mathcal{R}}\int_0^{t_{\mathcal{R}+1}} \mathcal{S}^{\tau-1}(t_{\mathcal{R}+1} - \mathcal{S})^{\alpha-1}\mathcal{N}(V,N,\mathcal{S},t)d\mathcal{S}}, \quad (14)$$

By approximating the integrals above, along with the terms $\boldsymbol{\mathcal{S}^{\tau-1}\mathcal{V}}$ and $\boldsymbol{\mathcal{S}^{\tau-1}\mathcal{N}}$, one can derive the following simplified forms of these integrals:

$$\boldsymbol{V^{\mathcal{R}+1}(t) = V^0 + \frac{\tau(1-\alpha)t_{\mathcal{R}}{}^{\tau-1}}{\mathcal{AB}(\alpha)}\mathcal{V}(V^{\mathcal{R}},N^{\mathcal{R}},t_{\mathcal{R}}) + \mathcal{L}_1 \times \sum_{r=0}^{\mathcal{R}}\left[t_{\mathcal{R}}{}^{\tau-1}\mathcal{K}_1\mathcal{V}(V^{\mathcal{R}},N^{\mathcal{R}},t_{\mathcal{R}}) - t_{\mathcal{R}-1}{}^{\tau-1}\mathcal{K}_2\mathcal{V}(V^{\mathcal{R}-1},N^{\mathcal{R}-1},t_{\mathcal{R}-1})\right]}, \quad (15)$$

$$\boldsymbol{N^{\mathcal{R}+1}(t) = N^0 + \frac{\tau(1-\alpha)t_{\mathcal{R}}{}^{\tau-1}}{\mathcal{AB}(\alpha)}\mathcal{N}(V^{\mathcal{R}},N^{\mathcal{R}},t_{\mathcal{R}}) + \mathcal{L}_1 \times \sum_{r=0}^{\mathcal{R}}\left[t_{\mathcal{R}}{}^{\tau-1}\mathcal{K}_1\mathcal{N}(V^{\mathcal{R}},N^{\mathcal{R}},t_{\mathcal{R}}) - t_{\mathcal{R}-1}{}^{\tau-1}\mathcal{K}_2\mathcal{N}(V^{\mathcal{R}-1},N^{\mathcal{R}-1},t_{\mathcal{R}-1})\right]}, \quad (16)$$

where $\boldsymbol{\mathcal{L}_1 = \tau(\Delta t)^{\alpha}/\mathcal{AB}(\alpha)(\Gamma(\alpha+2))}$, $\boldsymbol{\mathcal{K}_1 = (\mathcal{R}+1-r)^{\alpha}(\mathcal{R}-r+2+\alpha) - (\mathcal{R}-r)^{\alpha}(\mathcal{R}-}$

$\boldsymbol{r+2+2\alpha}$) and $\mathcal{K}_1 = (\mathcal{R}+1-r)^{\alpha+1} - (\mathcal{R}-r)^{\alpha}(\mathcal{R}-r+1+\alpha)$.

5. RESULTS AND DISCUSSION

To investigate the advantages of incorporating fractal-fractional calculus into neuronal modeling, we numerically simulate the proposed FFMLM and compare its dynamic behavior with that of the classical integer-order model, as shown in Figures 3 to 22. The simulations are performed under identical initial conditions and parameter settings to ensure a consistent basis for comparison. The results demonstrate that the FFMLM captures a broader range of dynamic behaviors, including more realistic spike shapes, varied inter-spike intervals, and greater sensitivity to external stimuli. These features are less prominent—or entirely absent—in the classical integer-order model. Phase portrait analysis further emphasizes these differences, revealing that the FFMLM exhibits richer geometrical structures and a more nuanced representation of neuronal excitability. The FFMLM displays a wide spectrum of neuronal behaviors, including quiescent states, regular spiking, and bursting patterns, depending on the applied input current I_{app} and the values of the fractional order α and fractal order τ. Numerical simulations confirm that the FFMLM preserves the essential characteristics of the classical model but expresses these behaviors under different parameter regimes due to the incorporation of memory effects and fractal time scaling. In the following analysis, a representative range of physical parameters is considered. The detailed description of our outcomes is given below, highlighting how changes in fractional and fractal orders influence neuronal dynamics in various regimes.

5.1 Variation of V with saddle-node bifurcation of Limit Cycles

Figures 3, 5, 7, and 9 illustrate the variation of the membrane potential V associated with the occurrence of saddle-node bifurcations of limit cycles. The corresponding phase portraits, presented in Figures 4, 6, 8, and 10, depict the bifurcation structure for different values of the fractional order α, fractal order τ, and applied current I_{app}. For low applied currents $I_{app} = 10$, the system remains in a stable equilibrium, corresponding to a quiescent neuronal state, as shown in Figures 3(a)–3(d). Specifically, Figure 3(c) displays the membrane potential V over time for $\alpha = 0.9$ and $\tau = 0.8$, where the neuron remains at rest with only minimal fluctuations. As the applied current increases to $I_{app} = 45$ (Figures 5(a)–5(d), 6(a)–6(d)), the model undergoes a saddle-node bifurcation of limit cycles (SNLC), in which stable and unstable limit cycles collide and annihilate. Figure 6(a)–6(d) illustrates this transition in the phase plane V vs. N, where the nullclines intersect at a single stable point before the onset of bifurcation. At $I_{app} = 100$ (Figures 7(a)–7(d), 8(a)–8(d)), the SNLC is fully developed, with the system showing a distinct separation between quiescent and spiking states, as seen in Figures 8(a)–8(d). Notably, the fractional order α shifts the bifurcation threshold to higher values of I_{app} when compared to the classical (integer-order) model. This reflects the memory-dependent dynamics introduced by the fractional framework. For example, at $\alpha = 0.7$ and $\tau = 0.8$, the SNLC occurs at $I_{app} = 100$, whereas in the classical model, bifurcation occurs at approximately $I_{app} = 60$. This delay underscores the modulatory role of fractional derivatives in shaping neuronal excitability. The above outcomes are based on the following values of $g_{ca} = 4$ mS/cm^2, $g_K = 8$ mS/cm^2, $g_L = 2$ mS/cm^2, $V_{Ca} = 120\,mV$, $V_K = -84\,mV$, $V_L = -60\,mV$, $V_1 = -1.2\,mV$, $V_2 = 18\,mV$, $V_3 = 12\,mV$, $V_4 = 17.4\,mV$, and $\phi = 0.067$.

5.2 Variation of V with Hopf bifurcation

Figures 11, 13, and 15 illustrate the variation of the membrane potential V associated with the occurrence of a Hopf bifurcation. The corresponding phase portraits, shown in Figures 12, 14, and 16, depict the bifurcation structure for different values of the fractional order α, fractal order τ, and applied current I_{app}. A transition from a resting state to periodic spiking is observed as I_{app} crosses a critical threshold (Figures 11(a)–11(d)). For instance, with $\alpha = 0.9$ and $\tau = 0.9$, a Hopf bifurcation occurs at $I_{app} = 90$ (Figures 14(a)–14(d)), which is significantly higher than the classical threshold of approximately $I_{app} = 40$. The post-bifurcation dynamics display damped oscillations (Figure 12(a)–12(d)), a characteristic feature of fractional-order systems where the influence of past states modulates present behavior. This history-dependent dynamic is consistent with experimental findings in real neurons, which often exhibit firing rates influenced by prior activity. Additionally, Figure 14(c) demonstrates the phase portrait for $\alpha = 0.95$ and $\tau = 0.9$, where the system's trajectory spirals toward a stable limit cycle, marking the onset of sustained spiking activity. The above outcomes are based on the following

values of $g_{ca} = 4.4$ mS/cm^2, $g_K = 8$ mS/cm^2, $g_L = 2$ mS/cm^2, $V_{Ca} = 120\,mV$, $V_K = -84\,mV$, $V_L = -60\,mV$, $V_1 = -1.2\,mV$, $V_2 = 18\,mV$, $V_3 = 2\,mV$, $V_4 = 30\ mV$, and $\phi = 0.004$.

5.3 Variation of V with homoclinic bifurcation

Figures 17, 19, and 21 illustrate the variation of the membrane potential V associated with the occurrence of homoclinic bifurcations. The corresponding phase portraits, shown in Figures 18, 20, and 22, depict the underlying bifurcation structures for different values of the fractional order α, fractal order τ, and applied current I_{app}. At intermediate current levels $I_{app} = 20, 50, 80$), the system exhibits homoclinic bifurcations, as shown in Figures Figures 18, 20, and 22. In particular, for $I_{app} = 50$ (Figures 19(a)–19(d), 20(a)–20(d)), the collision between a saddle point and a limit cycle leads to infinite-period oscillations, as illustrated from these figures. This bifurcation behavior is influenced by the fractal order τ; for example, with $\tau = 0.7$, the homoclinic bifurcation occurs at $I_{app} = 50$, whereas in the classical case $\tau = 0.7$, it appears at $I_{app} = 40$. Figure 20(c) further demonstrates the phase portrait for $\alpha = 0.8$ and $\tau = 0.7$, where the trajectory closely approaches a homoclinic orbit, confirming the bifurcation. These results suggest that fractal time scaling introduces additional delays in neuronal response, effectively mimicking the latency and adaptive timescales observed in biological neural systems. The above outcomes are based on the following values of $g_{ca} = 4$ mS/cm^2, $g_K = 8$ mS/cm^2, $g_L = 2$ mS/cm^2, $V_{Ca} = 120\,mV$, $V_K = -84\,mV$, $V_L = -60\,mV$, $V_1 = -1.2\,mV$, $V_2 = 18\,mV$, $V_3 = 12\,mV$, $V_4 = 17.4\ mV$, and $\phi = 0.023$.

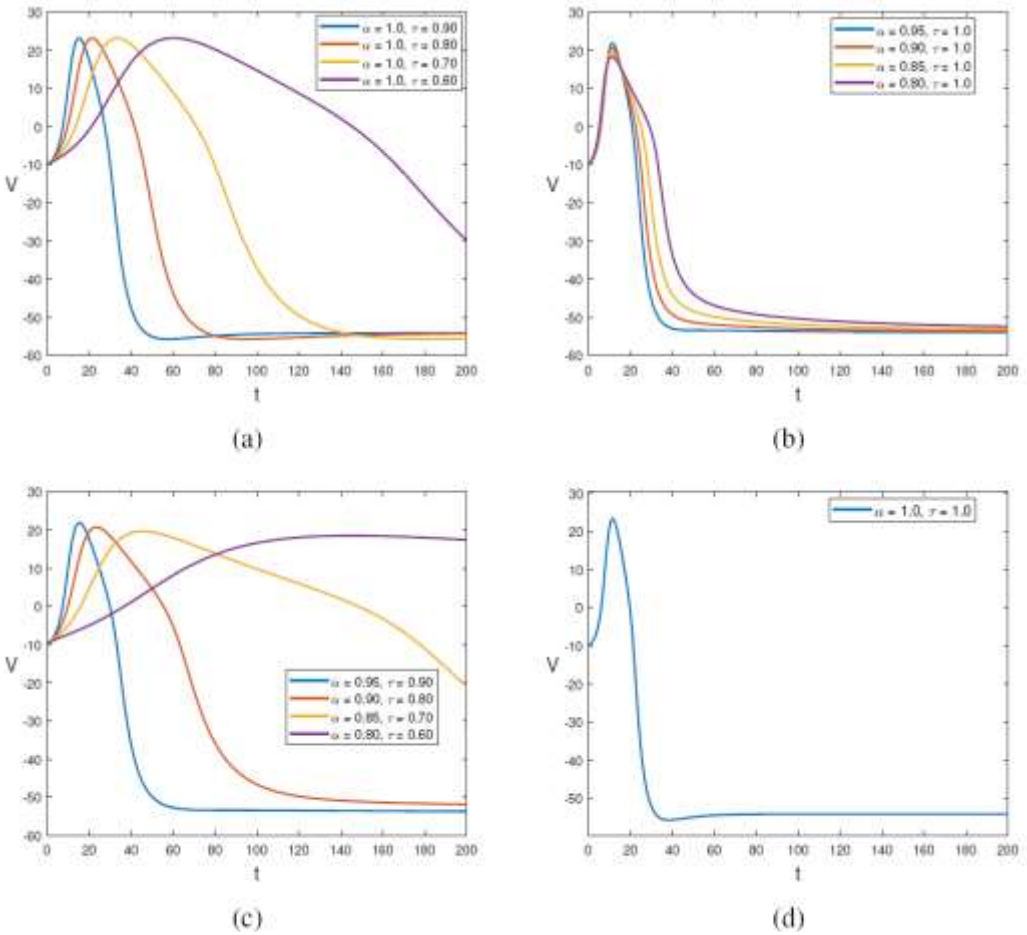

Fig. 3 Variation of V in the sense of (a) fractal, (b) fractional, (c) fractal-fractional, and (d) classical calculus based on occurrence of saddle node bifurcation of limit cycle or SNLC for $I_{app} = 10$.

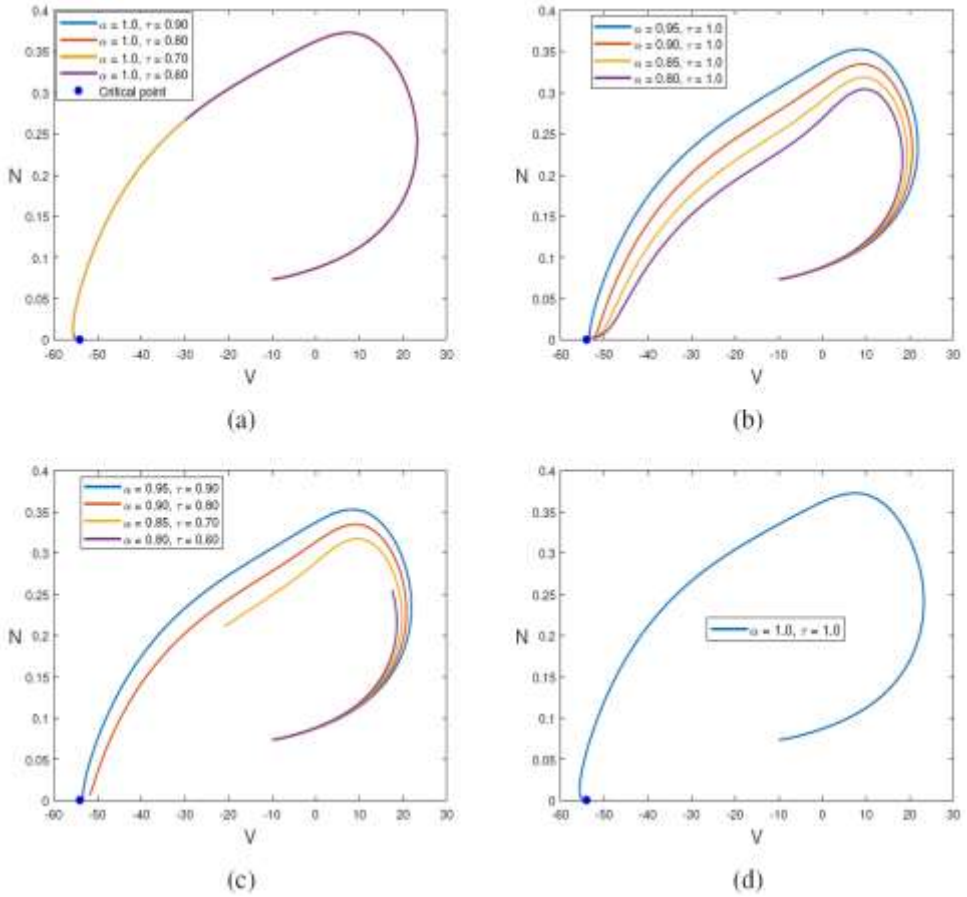

Fig. 4 A saddle-node bifurcation of limit cycles (SNLC) occurs at an applied current of $I_{app} = 10$ in the sense of (a) fractal, (b) fractional, (c) fractal-fractional, and (d) classical calculus.

5.4 Role of fractional and fractal parameters

The fractional order α governs the memory effect in the system, with lower values of α (e.g., $\alpha < 0.75$ delaying the onset of bifurcations and smoothing the transitions into spiking activity, as illustrated in Figures 13(a)–13(d). For instance, Figure 13(a) compares the membrane potential for $\alpha = 0.8$ and $\tau = 0.9$, showing a slower convergence to the limit cycle compared to the case with $\alpha = 0.9$. In contrast, the fractal dimension τ influences the time-scaling properties of the system. Higher values of τ (approximately 0.9) tend to sharpen the onset of bursting, as seen in Figures 15(a)–15(d). Specifically, Figure 15(b) shows that for $\tau = 0.9$, the spiking frequency increases abruptly at $I_{app} = 150$. The interplay between α and τ reveals novel dynamical regimes, such as intermittent bursting (Figure 19(d)), which emerges only for specific combinations of parameters (e.g., $\alpha = 0.8, \tau = 0.6$). This flexibility allows the model to replicate a wide range of neuronal behaviors without the need to modify the underlying biophysical parameters—a significant advantage over classical modeling approaches.

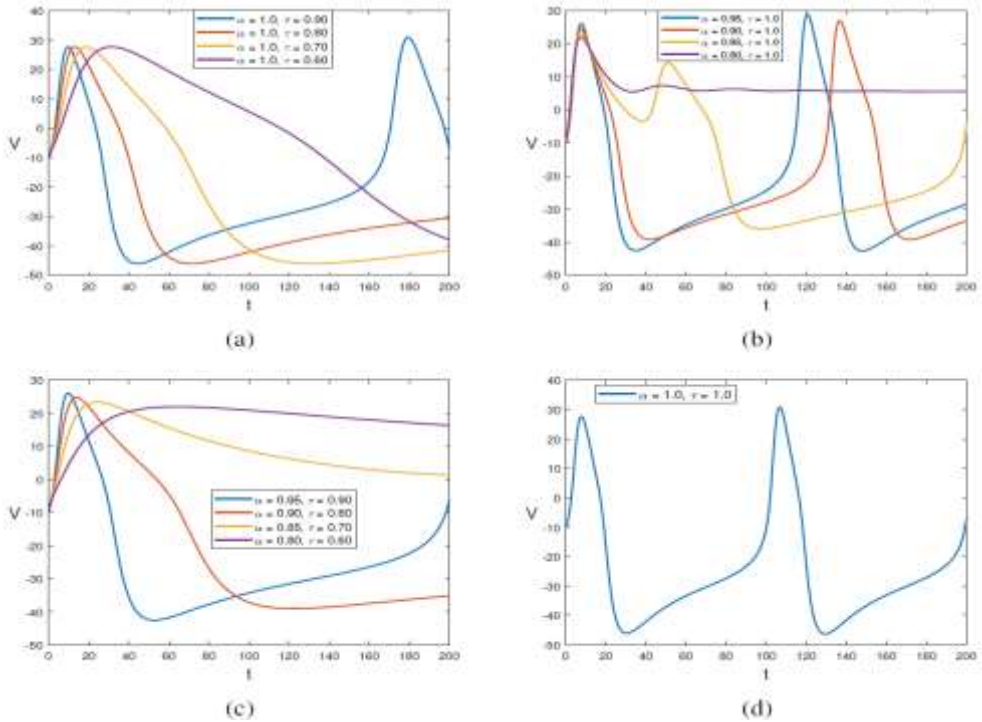

Fig. 5 Variation of V in the sense of (a) fractal, (b) fractional, (c) fractal-fractional, and (d) classical calculus based on occurrence of saddle node bifurcation of limit cycle or SNLC for $I_{app} = 45$.

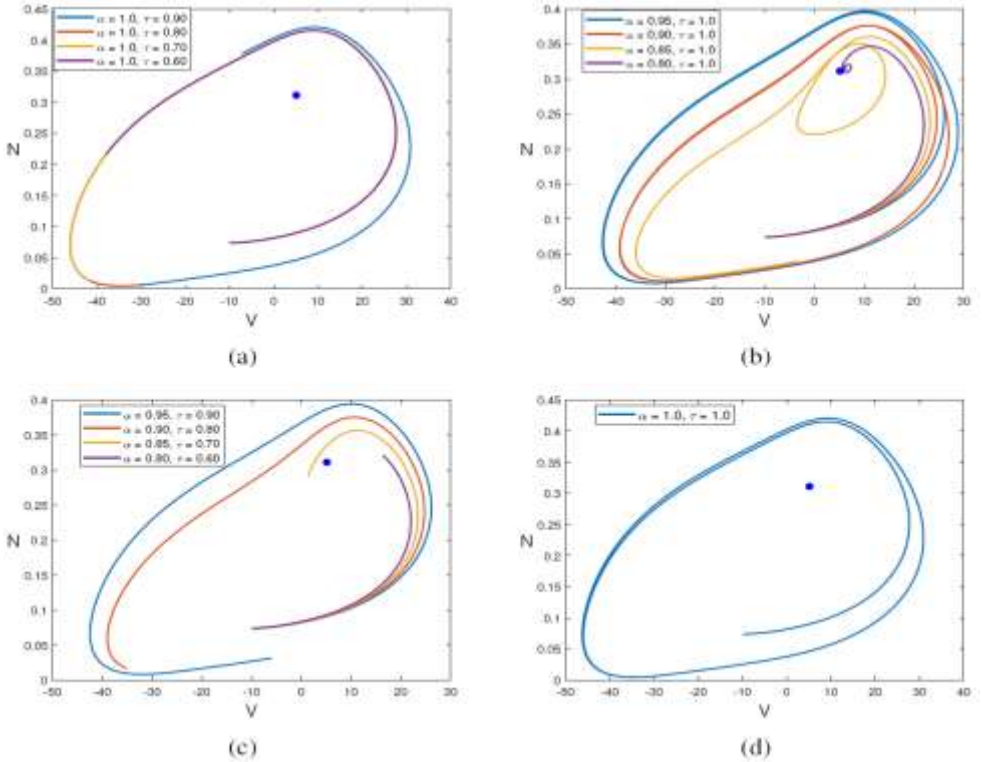

Fig. 6 A saddle-node bifurcation of limit cycles (SNLC) occurs at an applied current of $I_{app} = 45$ in the sense of (a) fractal, (b) fractional, (c) fractal-fractional, and (d) classical calculus

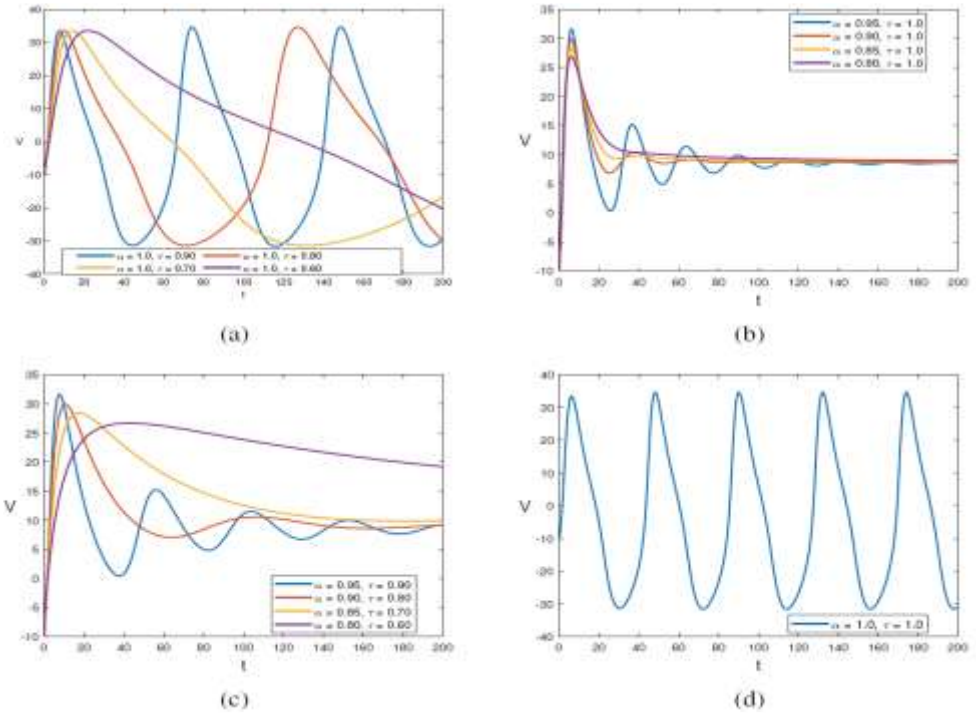

Fig. 7 Variation of V in the sense of (a) fractal, (b) fractional, (c) fractal-fractional, and (d) classical calculus based on occurrence of saddle node bifurcation of limit cycle or SNLC for $I_{app} = 100$.

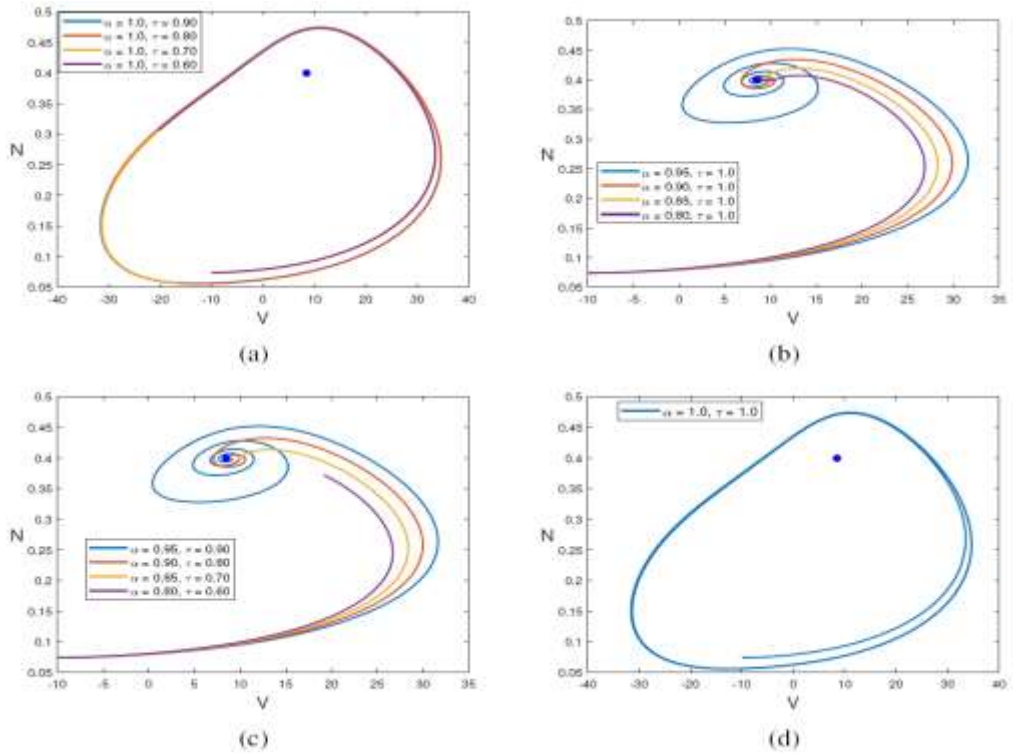

Fig. 8 A saddle-node bifurcation of limit cycles (SNLC) occurs at an applied current of $I_{app} = 100$ in the sense of (a) fractal, (b) fractional, (c) fractal-fractional, and (d) classical calculus

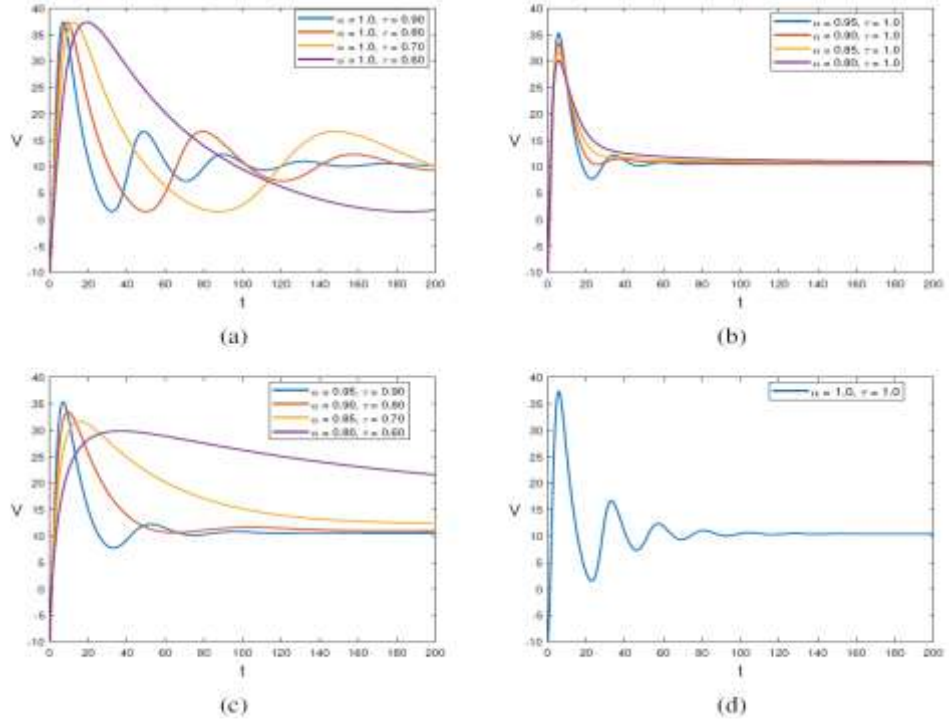

Fig. 9 Variation of V in the sense of (a) fractal, (b) fractional, (c) fractal-fractional, and (d) classical calculus based on occurrence of saddle node bifurcation of limit cycle or SNLC for $I_{app} = 140$.

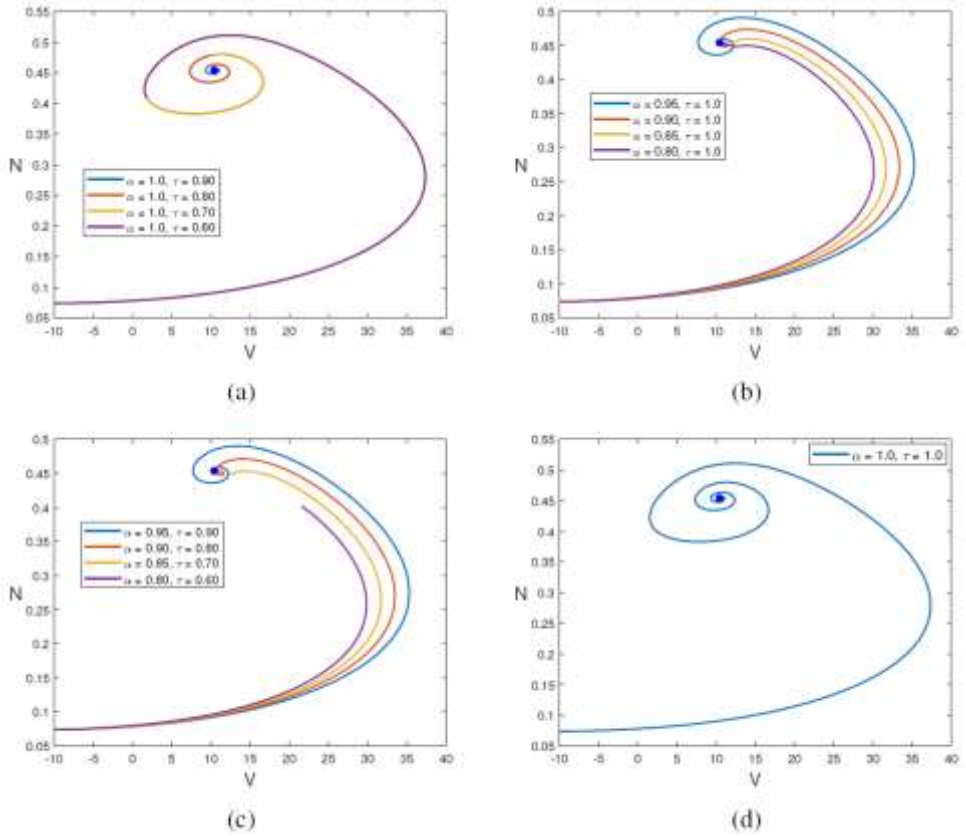

Fig. 10 A saddle-node bifurcation of limit cycles (SNLC) occurs at an applied current of $I_{app} = 140$ in the sense of (a) fractal, (b) fractional, (c) fractal-fractional, and (d) classical calculus.

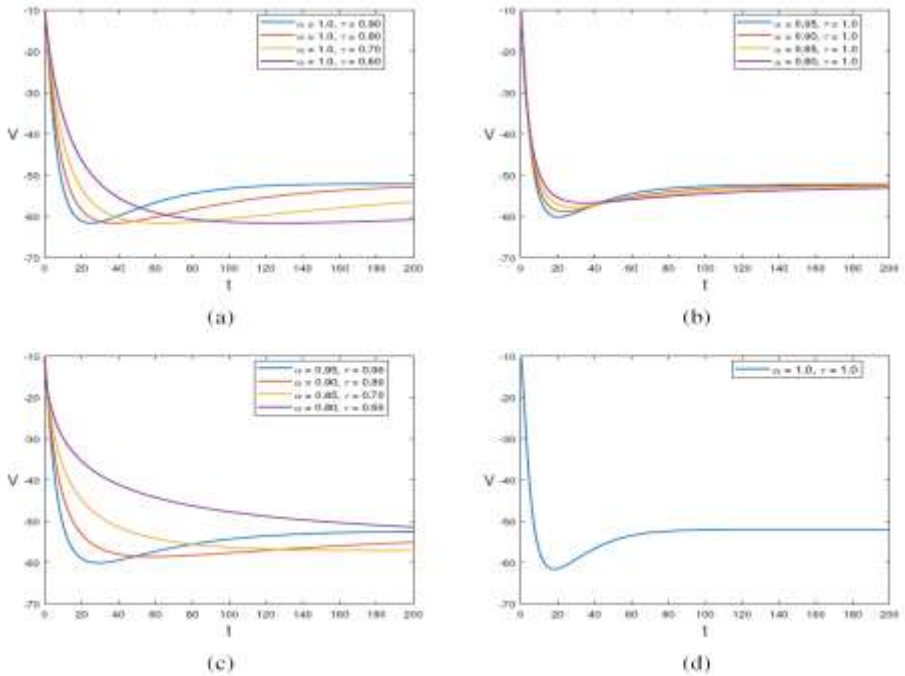

Fig. 11 Variation of V in the sense of (a) fractal, (b) fractional, (c) fractal-fractional, and (d) classical calculus based on occurrence of hopf bifurcation for $I_{app} = 20$.

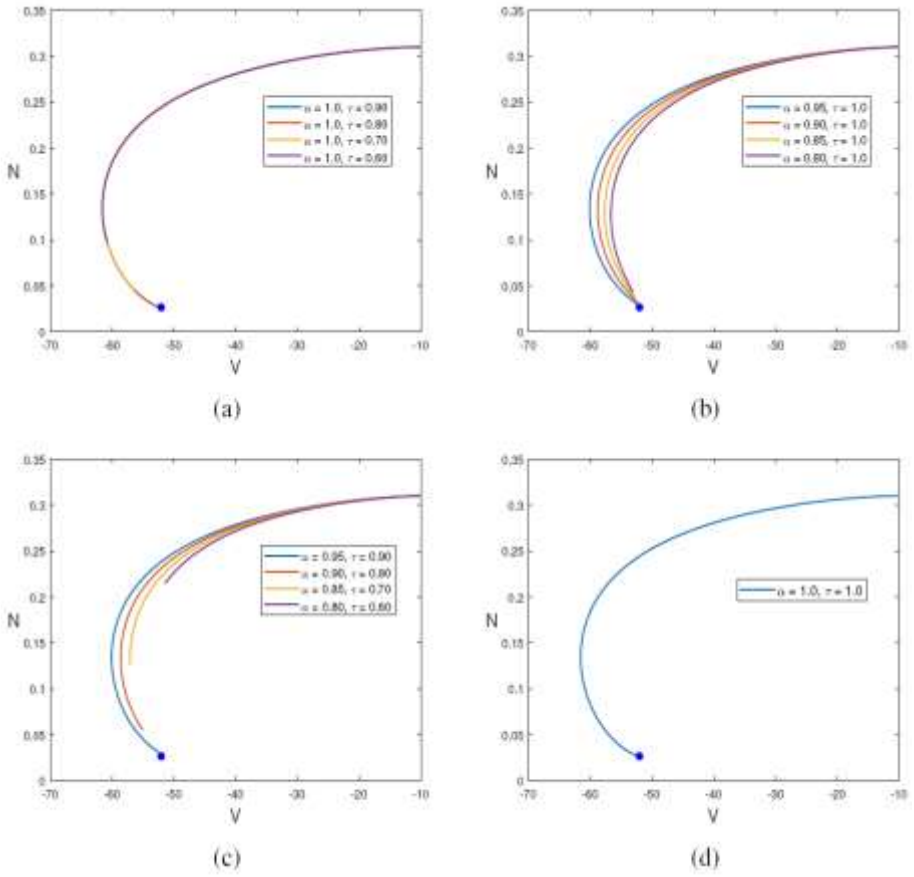

Fig. 12 A hopf bifurcation occurs at an applied current of $I_{app} = 20$ in the sense of (a) fractal, (b) fractional, (c) fractal-fractional, and (d) classical calculus.

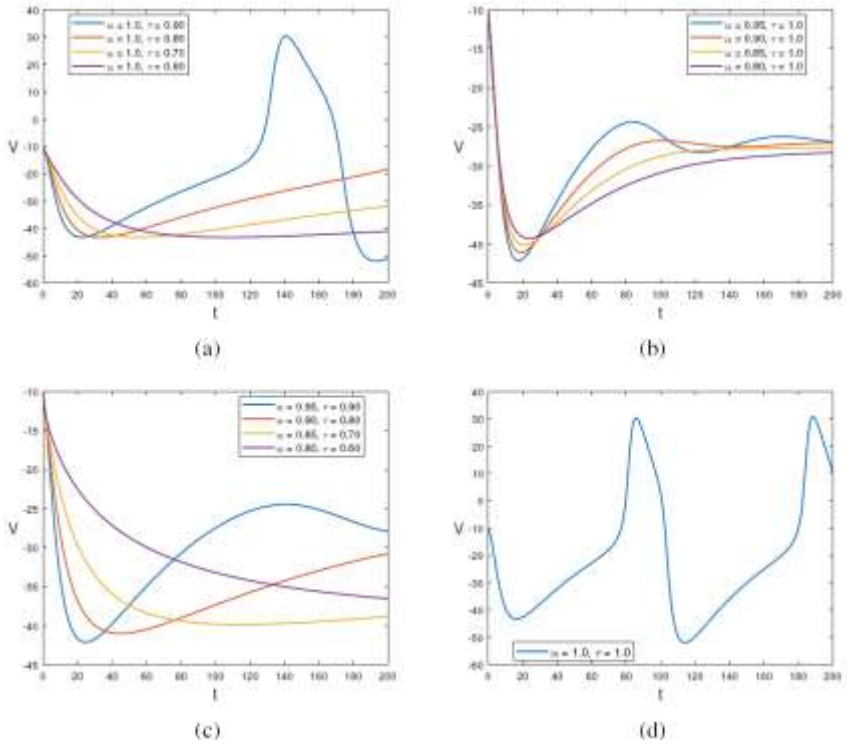

Fig. 13 Variation of V in the sense of (a) fractal, (b) fractional, (c) fractal-fractional, and (d) classical calculus based on occurrence of hopf bifurcation for $I_{app} = 90$.

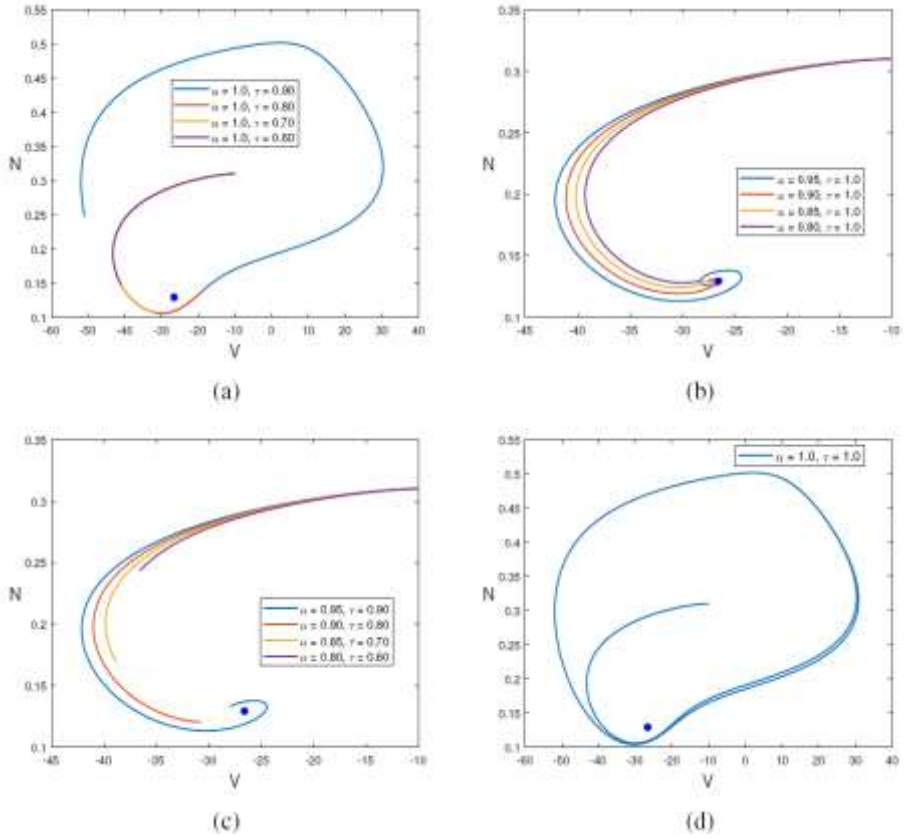

Fig. 14 A hopf bifurcation occurs at an applied current of $I_{app} = 90$ in the sense of (a) fractal, (b) fractional, (c) fractal-fractional, and (d) classical calculus.

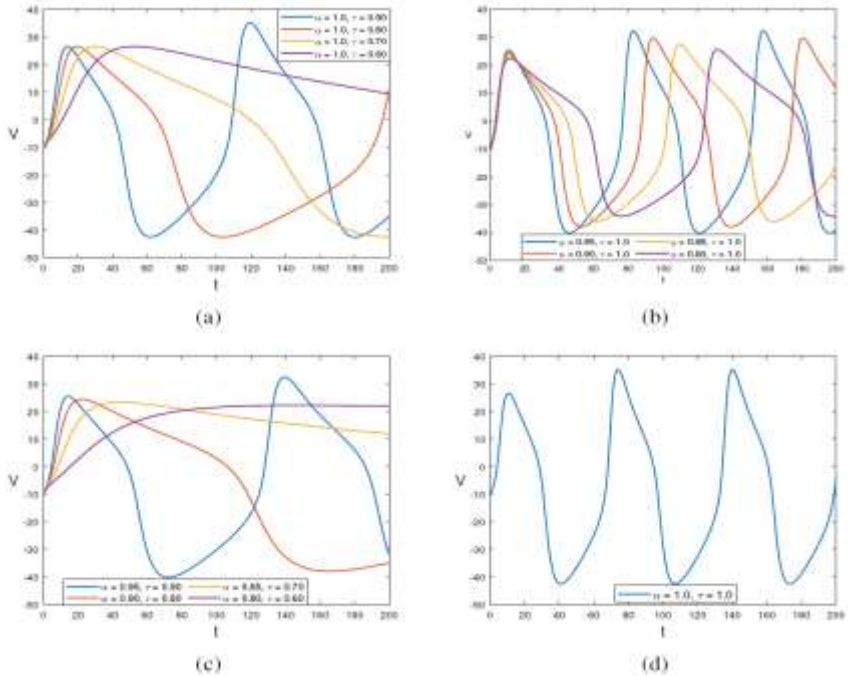

Fig. 15 Variation of V in the sense of (a) fractal, (b) fractional, (c) fractal-fractional, and (d) classical calculus based on occurrence of hopf bifurcation for $I_{app} = 150$.

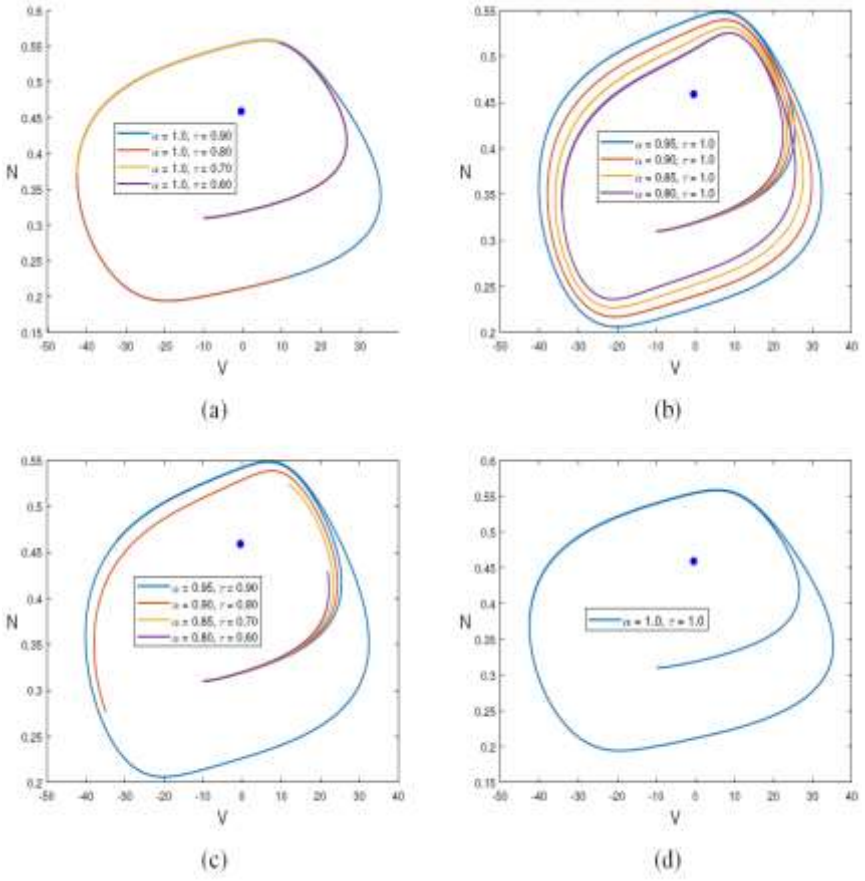

Fig. 16 A hopf bifurcation occurs at an applied current of $I_{app} = 150$ in the sense of (a) fractal, (b) fractional, (c) fractal-fractional, and (d) classical calculus.

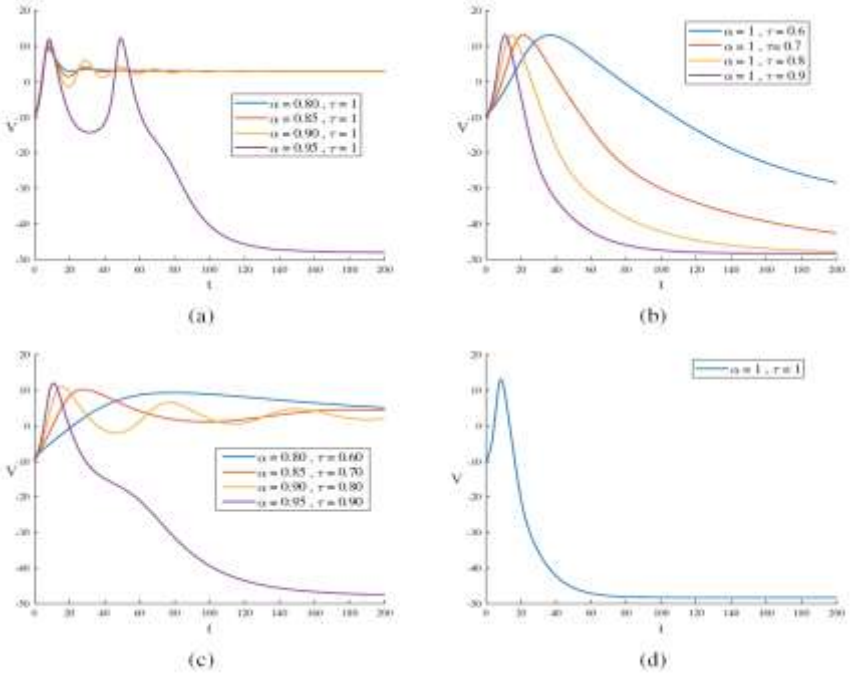

Fig. 17 Variation of V in the sense of (a) fractal, (b) fractional, (c) fractal-fractional, and (d) classical calculus based on occurrence of Homoclinic bifurcation for $I_{app} = 20$.

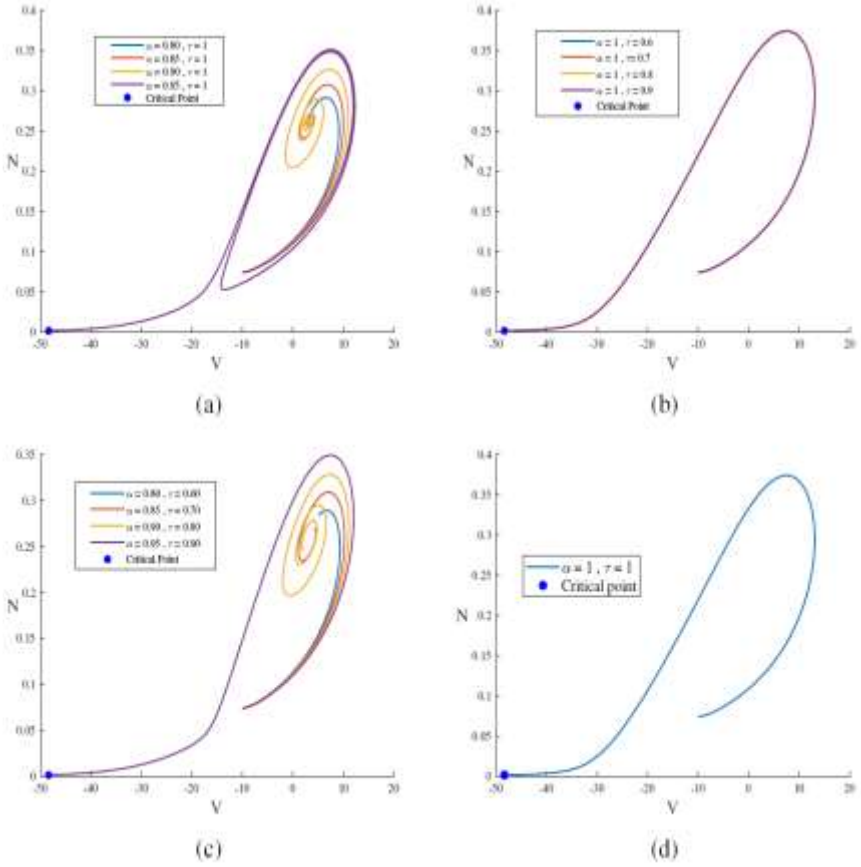

Fig. 18 Phase diagrams with the occurrence of Homoclinic bifurcation at an applied current of $I_{app} = 20$ in the sense of (a) fractal, (b) fractional, (c) fractal-fractional, and (d) classical calculus.

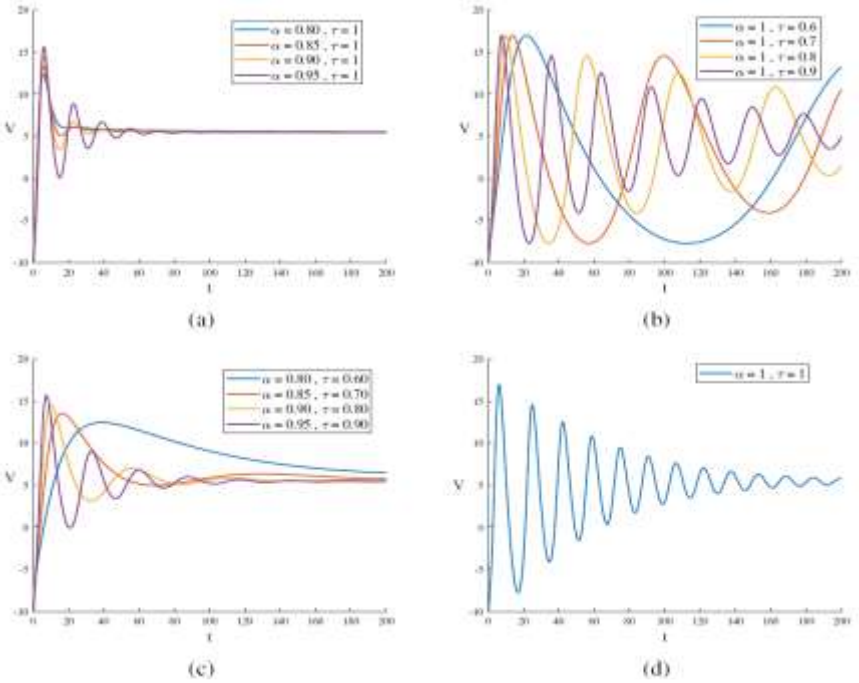

Fig. 19 Variation of V in the sense of (a) fractal, (b) fractional, (c) fractal-fractional, and (d) classical calculus based on occurrence of Homoclinic bifurcation for $I_{app} = 50$.

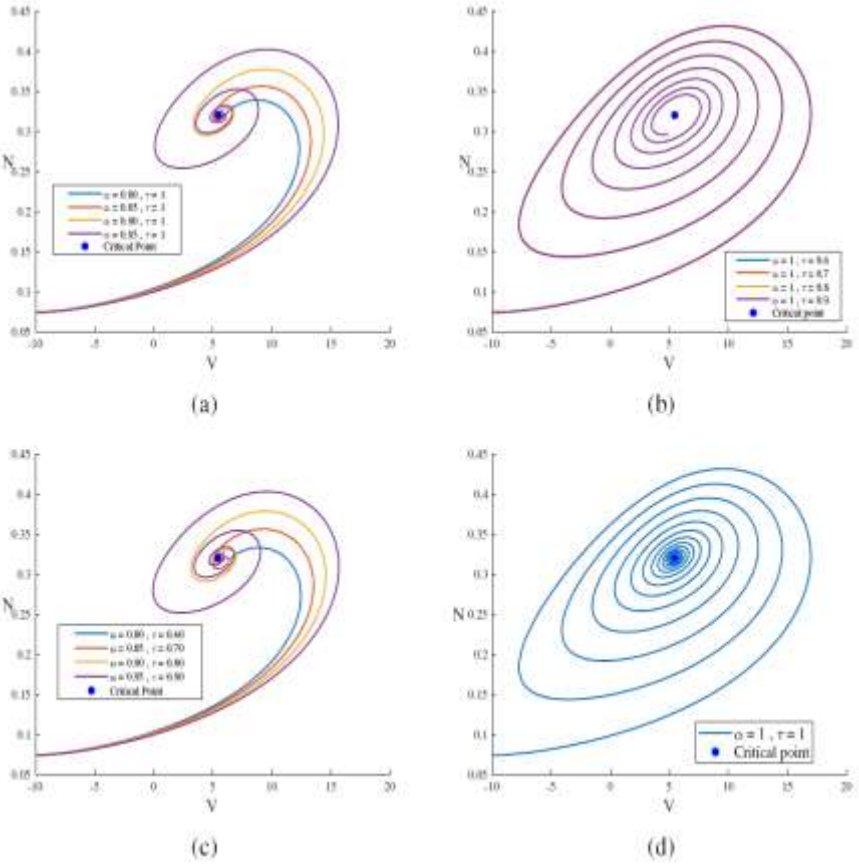

Fig. 20 Phase diagrams with the occurrence of Homoclinic bifurcation at an applied current of $I_{app} = 50$ in the sense of (a) fractal, (b) fractional, (c) fractal-fractional, and (d) classical calculus.

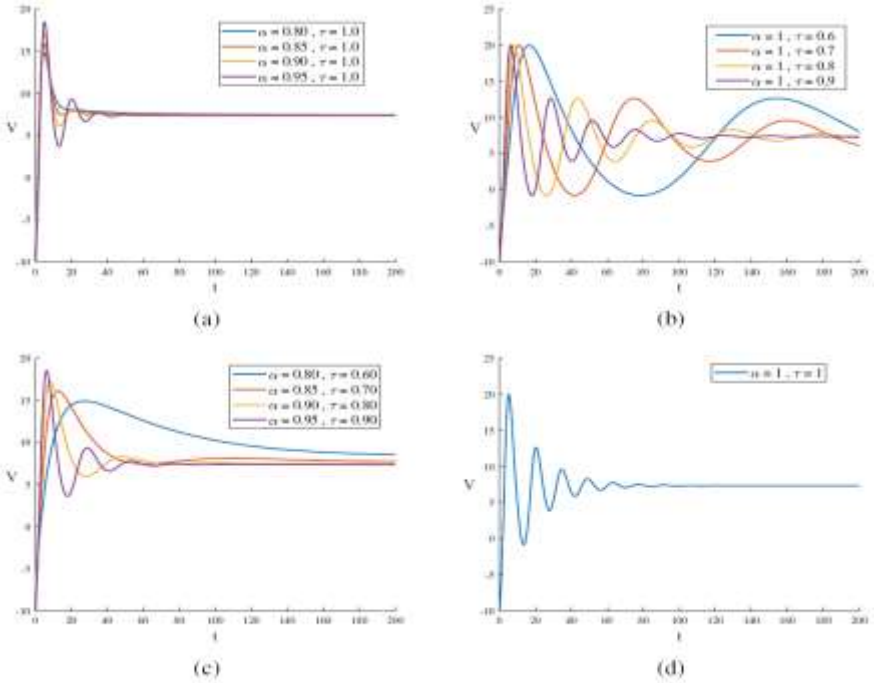

Fig. 21 Variation of V in the sense of (a) fractal, (b) fractional, (c) fractal-fractional, and (d) classical calculus based on occurrence of Homoclinic bifurcation for $I_{app} = 80$.

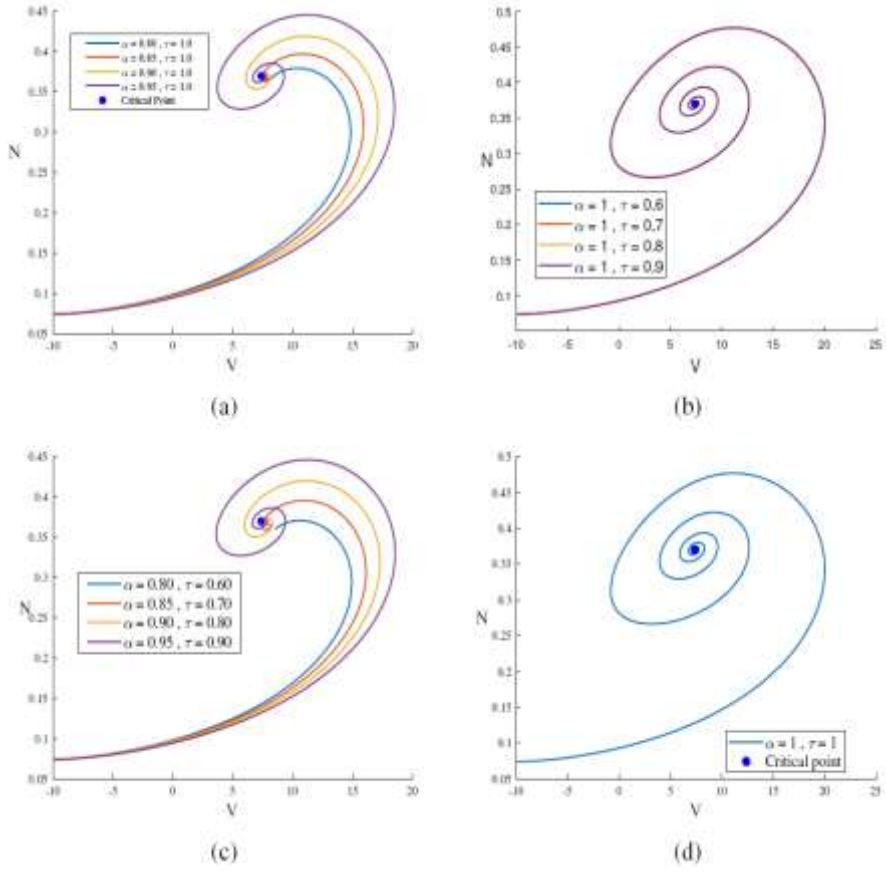

Fig. 22 Phase diagrams with the occurrence of Homoclinic bifurcation at an applied current of $I_{app} = 80$ in the sense of (a) fractal, (b) fractional, (c) fractal-fractional, and (d) classical calculus.

5.5 Comparison with classical model incorporating with and without GL fractional derivative

While the integer-order Morris–Lecar model effectively captures basic neuronal excitability, the fractal–fractional Morris–Lecar (FFML) model offers a more nuanced and flexible representation of neuronal dynamics. Notably, the classical model assumes a single timescale for adaptation, whereas the FFML framework inherently incorporates multiple timescales through its fractional and fractal parameters. This distinction is evident from Figures that displayed in this work, where the FFMLM demonstrates richer dynamics. For instance, Figure 11(c) and 12 (c) illustrates that, for $\alpha = 0.85$ and $\tau = 0.7$, the neuron exhibits both fast spiking and slow subthreshold oscillations—behavior not captured by the integer-order model. Moreover, the FFMLM can reproduce complex firing patterns, including chaotic activity, as shown in Figure 20(a)-20(d) and 21(a)-21(d), by adjusting α and τ under otherwise fixed conditions. This capability is absent in the classical model and aligns well with experimental observations of neurons displaying both periodic and chaotic spiking within similar physiological regimes. These findings underscore the FFML model's potential to more accurately reflect the variability and complexity of real neuronal systems. However, Although Azizi [21] utilized the GL fractional derivative to generalize the Morris-Lecar model and analyzed the neuronal dynamics. The GL fractional derivative, while foundational in fractional calculus, is limited by its singular kernel, sensitivity to noise, and high computational cost due to its reliance on long memory and backward differences. It struggles with modeling real-world systems that exhibit complex, nonlocal, or heterogeneous behavior. In contrast, the Atangana–Baleanu (AB) fractal-fractional derivative addresses these limitations by using a non-singular Mittag-Leffler kernel and incorporating fractal dimensions, enabling it to model systems with realistic memory effects and structural complexity more accurately and stably.

6. CONCLUSION

This study extends the classical Morris–Lecar neuronal model into the fractal–fractional domain using the Atangana–Baleanu derivative, enabling the incorporation of both memory effects and fractal time scaling. The proposed FFMLM model demonstrates significant enhancements over the traditional integer-order model by capturing a wider spectrum of neuronal behaviors. Key outcomes include the delayed onset of bifurcations such as SNLC, Hopf, and homoclinic types, with these transitions occurring at higher input currents due to the influence of fractional and fractal parameters. The model also reveals new dynamical regimes, including intermittent bursting and chaotic firing, which do not arise in the classical framework. Furthermore, the FFML model successfully reproduces biologically relevant phenomena such as multi-timescale adaptation and history-dependent firing patterns, offering a more faithful representation of real neuronal dynamics.

These results underscore the value of incorporating fractional and fractal dynamics into neural modeling, particularly for studying complex behaviors and pathological states like epilepsy. The ability to tune neuronal excitability through the parameters α and τ offers potential applications in neuromorphic system design, where adaptable and programmable firing patterns are essential. Future work could explore network-level simulations to study collective dynamics, validate the model with experimental data from neurons exhibiting fractional characteristics, and implement the model in efficient hardware platforms. Overall, the FFMLM provides a powerful and flexible framework for advancing theoretical neuroscience and developing bio-inspired technologies.

Conflict of interest: No conflict of interest.

REFERENCES

[1] Izhikevich, E. M. (2007). *Dynamical Systems in Neuroscience*. MIT Press.

[2] Izhikevich, E. M. (2004). Which model to use for cortical spiking neurons? *IEEE Transactions on Neural Networks, 15*(5), 1063–1070.

[3] Izhikevich, E. M. (2003). Simple model of spiking neurons. *IEEE Transactions on Neural Networks, 14*(6), 1569–1572.

[4] Izhikevich, E. M. (2000). Neural excitability, spiking and bursting. *International Journal of Bifurcation and Chaos, 10*(6), 1171–1266.

[5] Hodgkin, A. L. (1948). The local electric changes associated with repetitive action in a non-medullated axon. *Journal of Physiology, 107*, 165–181.

[6] Hodgkin, A. L., & Huxley, A. F. (1952). A quantitative description of membrane current and its application to conduction and excitation in nerve. *Journal of Physiology, 117*, 500–544.

[7] Azizi, T. (2021). *Mathematical Modeling with Applications in Biological Systems, Physiology, and Neuroscience*. Kansas State University.

[8] Rinzel, J., & Ermentrout, G. B. (1998). Analysis of neural excitability and oscillations. In *Methods in Neuronal Modeling*. MIT Press.

[9] Ermentrout, G. B., & Terman, D. H. (2010). *Mathematical Foundations of Neuroscience*. Springer.

[10] Ermentrout, B. (1996). Type I membranes, phase resetting curves, and synchrony. *Neural Computation, 8*(5), 979–1001.

[11] Kosmidis, K., & Macheras, P. (2018). On the dilemma of fractal or fractional kinetics in drug release studies: A comparison between Weibull and Mittag-Leffler functions. *International Journal of Pharmaceutics, 43*, 269.

[12] He, J.-H. (2018). Fractal calculus and its geometrical explanation. *Results in Physics, 10*, 272.

[13] Nottale, L. (1988). On time in microphysics. *Comptes Rendus de l'Académie des Sciences II, 306*, 341–346.

[14] Moaddy, K., Radwan, A. G., Salama, K. N., Momani, S., & Hashim, I. (2012). The fractional-order modeling and synchronization of electrically coupled neuron systems. *Computers & Mathematics with Applications, 64*(10), 3329–3339.

[15] Malik, S. A., & Mir, A. H. (2020). FPGA realization of fractional order neuron. *Applied Mathematical Modelling, 81*, 372–385.

[16] Shi, M., & Wang, Z. (2014). Abundant bursting patterns of a fractional-order Morris–Lecar neuron model. *Communications in Nonlinear Science and Numerical Simulation, 19*(6), 1956–1969.

[17] Jun, D., Guang-jun, Z., Yong, X., Hong, Y., & Jue, W. (2013). Dynamic behavior analysis of fractional-order Hindmarsh–Rose neuronal model. *Cognitive Neurodynamics, 8*, 167–175.

[18] Wang, Z., Wang, X., Li, Y., & Huang, X. (2017). Stability and Hopf bifurcation of fractional-order complex-valued single neuron model with time delay. *International Journal of Bifurcation and Chaos, 27*(9), 1750209.

[19] Mondal, A., Sharma, S. K., Upadhyay, R. K., & Mondal, A. (2019). Firing activities of a fractional-order FitzHugh–Rinzel bursting neuron model and its coupled dynamics. *Scientific Reports, 9*, 15721.

[20] Tolba, M. F., Elsafty, A. H., Armanyos, M., Said, L. A., Madian, A. H., & Radwan, A. G. (2019). Synchronization and FPGA realization of fractional-order Izhikevich neuron model. *Microelectronics Journal, 89*, 56–69.

[21] Azizi, T. (2023). Analysis of neuronal oscillations of fractional-order Morris–Lecar model. *European Journal of Mathematical Analysis, 3*(2).

[22] Delkhosh, M. (2013). Introduction of derivatives and integrals of fractional order and its applications. *Applied Mathematics and Physics, 1*, 103.

[23] Caputo, M., & Fabrizio, M. (2015). A new definition of fractional derivative without singular kernel. *Progress in Fractional Differentiation and Applications, 1*, 73.

[24] Abdeljawad, T. (2015). On conformable fractional calculus. *Journal of Computational and Applied Mathematics, 279*, 57.

[25] Uddin, M. F., Hafez, M. G., Hwang, I., & Park, C. (2022). Effect of space fractional parameter on nonlinear ion acoustic shock wave excitation in an unmagnetized relativistic plasma. *Frontiers in Physics, 9*, 766035.

[26] Atangana, A., & Qureshi, S. (2019). Modeling attractors of chaotic dynamical systems with fractal–fractional operators. *Chaos, Solitons & Fractals, 123*, 320.

[27] Abro, K. A., Memon, I. Q., Yousef, A., & Al-Mdallal, Q. M. (2025). A comparative analysis of fractal and fractionalized thermal non-equilibrium model for chaotic convection saturated by porous medium. *South African Journal of Chemical Engineering, 51*, 124.

[28] Abro, K. A., & Atangana, A. (2024). Mathematical modeling of neuron model through fractal–fractional differentiation based on Maxwell electromagnetic induction: Application to neurodynamics. *Neural Computing and Applications, 36*, 18377.

[29] Abro, K. A., & Atangana, A. (2023). Strange fractal attractors and optimal chaos of memristor–memcapacitor via non-local differentials. *Qualitative Theory of Dynamical Systems, 22*, 156.

[30] Iqbal, S. A., Hafez, M. G., Chu, Y.-M., & Park, C. (2022). Dynamical analysis of nonautonomous RLC circuit with the absence and presence of Atangana–Baleanu fractional derivative. *Journal of Applied Analysis and Computation, 12*(2), 770–789.

[31] Morris, C., & Lecar, H. (1981). Voltage oscillations in the barnacle giant muscle fiber. *Biophysical Journal, 35*(1), 193–213.

[32] Azizi, T., & Alali, B. (2020). Impact of chloride channel on spiking patterns of Morris–Lecar model. *Applied Mathematics, 11*(7), 650–669.

[33] Qi, G., Wu, Y., & Hu, J. (2021). Abundant firing patterns in a memristive Morris–Lecar neuron model. *International Journal of Bifurcation and Chaos, 31*(13), 2150170.